Insights on phase formation from thermodynamic calculations and machine learning of 2436 experimentally measured high entropy alloys

Chuangye Wang 1, Wei Zhong 1, Ji-Cheng Zhao 1,*

¹ Department of Materials Science and Engineering, University of Maryland, College Park, MD 20742, USA

*Corresponding authors. Email addresses: jczhao@umd.edu (J.-C. Zhao)

Abstract

Both CALPHAD (CALculation of PHAse Diagrams) and machine-learning (ML) approaches were employed to analyze the phase formation in 2,436 experimentally measured high entropy alloy (HEA) compositions consisting of various quinary mixtures of Al, Co, Cr, Cu, Fe, Mn, and Ni. CALPHAD was found to have good capabilities in predicting the BCC/B2 and FCC phase formation for the 1,761 solid-solution-only compositions, excluding HEAs containing an amorphous phase (AM) or/and intermetallic compound (IM). Phase selection rules were examined systematically using several parameters and it revealed that valency electron concentration (VEC) < 6.87 and VEC > 9.16 are the conditions for the formation of single-phase BCC/B2 and FCC, respectively; and CALPHAD could predict this with essentially 100% accuracy. Both CALPHAD predictions and experimental observations show that more BCC/B2 alloys are formed over FCC alloys as the atomic size difference between the elements increases. Four machine learning (ML) algorithms, decision tree (DT), k-nearest neighbor (KNN), support vector machine (SVM), and artificial neural network (ANN), were employed to study the phase selection rules for two different datasets, one consisting of 1,761 solid-solution (SS) HEAs without AM and/or IM phases, and the other set consisting of all the 2,436 HEA compositions. Cross validation (CV) was performed to optimize the ML models and the CV accuracies are found to be 91.4%, 93.1%, 90.2%, 89.1% for DT, KNN, SVM, and ANN respectively in predicting the formation of BCC/B2, BCC/B2 + FCC, and FCC; and 93.6%, 93.3%, 95.5%, 92.7% for DT, KNN, SVM, and ANN respectively in predicting SS, AM, SS + AM, and IM phases. Sixty-six experimental bulk alloys with SS structures are predicted with trained ANN model, and the accuracy reaches 81.8%. VEC is found to be most important parameter in phase prediction for BCC/B2, BCC/B2 + FCC, and FCC phases. Electronegativity difference and FCC-BCC-index (FBI) are the two additional dominating features in determining the formation of SS, AM, SS + AM, and IM. A separation line $\Delta H_{mix} = 28.97 \times VEC - 246.77$ was found in the VEC-vs- ΔH_{mix} plot to predict the formation of single-phase BCC/B2 or FCC with a 96.2% accuracy (ΔH_{mix} = mixing enthalpy). These insights will be very valuable for designing HEAs with targeted crystal structures.

Keywords: High entropy alloys, CALPHAD, high-throughput calculations, phase selection rules, machine learning.

1. Introduction

High entropy alloys (HEAs) typically consist of four or more principal elements with concentration between 5 and 35 at.% [1–10] in contrast to traditional alloys such as copper, iron, magnesium and aluminum alloys with low concentrations of other alloying elements. HEAs open up vast composition spaces for designing and discovering new alloys for ever-increasing demands of new materials for energy, environment, and human well-beings.

There are many experimental methods for preparation of HEAs, including mechanical alloying, induction melting, vacuum arc melting, vapor deposition method, and sputtering [3,5,11–15]. To accelerate the discovery of novel and advanced materials, the CALculation of PHAse Diagrams (CALPHAD) approach has often been employed to predict and investigate phase formation of HEAs [16-24]. In addition to CALPHAD, phase selection rules were developed by various research groups to help predict phases of HEAs via studying the existing experimental data. Such empirical rules are built by presenting the formation of phases in onedimensional histograms or two-dimensional plots whose axes are usually thermodynamic and physical parameters. For instance, the Hume-Rothery rules depict the effects of atomic size ratio and electrochemical properties on solid solution (SS) formation [25]. Guo et al. revealed that single-phase FCC forms at valency electron concentration (VEC) > 8 and single-phase BCC forms at VEC < 6.87, while Jiang's work added some constraints based on their designed alloys and indicated that this formation rule applies under the conditions of $\Delta S_{mix} > 12.47$, 7.27kJ/mol $< \Delta H_{mix} < 4$ kJ/mol, and $\delta < 4.27\%$, where ΔS_{mix} , ΔH_{mix} , and δ are the mixing entropy, mixing enthalpy, and difference in atomic sizes, respectively [26,27]. Recently, Yang et al. developed a new VEC selection rule for predicting SS phases based on high-throughput CALPHAD calculations in the Al-Co-Cr-Fe-Ni system [28]. Other parameters such as -22 $\leq \Delta H_{mix} \leq 7$ kJ/mol, $0 \leq \delta \leq 8.5$, and $11 \leq \Delta S_{mix} \leq 19.5$ kJ/mol are found to be conditions for the formation of SS [29]. According to the evaluation of Senkov et al. over 130,000 alloys, the increasing number of alloying elements in a system beyond 3 results in a reduced likelihood of occurrence of SS [30]. Inoue summarized the conditions to form bulk metallic glasses (BMGs) in terms of the number of elements, atomic size ratios, and mixing heat of atomic pairs [31]. Both $\Omega \ge 1.1$ and $\delta \le 6.6\%$ were shown by Yang and Zhang to be conditions for the formation of SS phases, and BMGs form in regions of smaller Ω and larger δ as compared to HEAs, where Ω is a parameter related to the ΔH_{mix} , ΔS_{mix} , and melting temperature (T_m) of constituent elements [32]. A single dimensionless thermodynamic parameter ϕ which is correlated with ΔH_{mix} , ΔS_{mix} , T_m , and excessive entropy was defined and HEAs were found to be single-phase SS (SPSS) at ϕ > 20 based on the analysis of nearly 50 types of HEAs [33]. All these phase selection rules can be used to guide future design of HEAs; however, most of the rules were developed from small experimental datasets. Li and Tsai collected 100 selected HEAs from the literature and assessed the accuracies of 8 published formation rules; they found that the overall accuracy is only ~ 72% in predicting SPSSs and intermetallics (IM) [34]. Therefore, it is highly desirable to test and expand these rules using very large, consistent datasets.

Machine learning (ML) holds great promise for future materials design and discovery [35,36]. Unlike CALPHAD that was built upon semi-empirical physical models, ML makes prediction using data-driven strategies with unique algorithms [6,37,38] that learn from training datasets with input patterns and a optimization target, and then extract the implicit insights

hidden in the datasets. For phase prediction using ML, the properties of alloys or constituent atoms will be taken as input features, and the crystal structures of the phases are the corresponding targets. Since ML can explore different features simultaneously, it is able to overcome the limitations of traditional strategies in studying phase selection rules [39-41]. For example, phase selection rules was explored via support vector machine (SVM) and artificial neural network (ANN) on two separate group of features - compositions of HEAs and physical parameters of HEAs, respectively, and showed that the accuracies of learning obtained from these two groups of input features are similar and high for HEAs when 4 or 5 physical parameters were employed [42,43]. The Gaussian process statistical analysis was performed on 322 alloys based on a combination of 9 physical parameters, which provided a robust predictions for the formation of SPSSs [44]. Krishna et al. utilized six ML approaches with 5 input features to study the classification of SS and SS + IM with a dataset of 636 compositions. and they found that the trained ANN reached 80% prediction accuracy and can correctly predict the crystal structures of newly designed alloys [45]. Zhao et al. recently studied 3 categories (SS, IM, SS + IM) using five ML models and achieved 87% prediction accuracy through ANN with 5 selected features [46]. Pei et al. put forward a new parameter λ related to bulk modulus. melting temperature, volume, and configurational entropy with the help of performing ML and found that SPSS forms at $\lambda \ge 1$ with 73% accuracy and it can increase to 81% with a constraint of $\delta \le 6\%$. They further applied their new formation rule to new compositions that are SPSSs predicted by CALPHAD and the consistency reached 94% [47]. In addition to studying phase formation separately, a recent study applied the eXtreme Gradient Boosting (XGBoost) model to explore > 300,000 equilibrium data of HEAs generated by CALPHAD calculations, and built more comprehensive and superior phase selection rules for single-phase FCC and BCC based on the 5 ML-selected features [48]. Machaka applied 6 ML models to 896 SPSSs and 101 dualphase SSs and did feature selection using 36 dataset features [49]. The accuracy reaches 95% with the top-most identified 13 features. Zhang et al used a model of SVM combined Kernel Principal Component Analysis to classify a dataset of 556 entries including SS, amorphous (AM), the mixture of SS and IM, and IM, and obtained 97% accuracy with 4 selected features [50]. Zhou et al. performed various experiments on the (FeCrNi)_{10-x}(ZrCu)_x system to verify the ability of the trained ML models, and they achieved good agreements for bulk alloys made by arc melting and ribbon samples through vacuum melt spinning. The thin films made via cosputtering presented a transition from a crystalline to amorphous structure as x in (FeCrNi)₁₀₋ _x(ZrCu)_x increases, which is consistent with their ML predictions [51].

Table 1. Summary of experimental alloys classified by the phases [15].

Phase	Number
BCC	604
B2	158
FCC	553
BCC + FCC	441
B2 + FCC	5
BCC + Amorphous	71
FCC + Amorphous	145

BCC + FCC + Amorphous	34	
Amorphous	192	
Intermetallic compound (σ and/or more)	233	

Experimental data of 2,436 quinary HEAs with different mixtures of Al, Cr, Mn, Fe, Co, Ni, Cu from Kube et al. [15] were employed in this study to perform a more extensive test of CALPHAD predictions and ML capabilities. The phase categories and their corresponding numbers of alloys are listed in **Table 1**. CALPHAD was utilized to calculate the phase equilibrium of 1,761 SS HEAs from a full dataset of 2,436 HEAs, and the CALPHAD predictions were analyzed and compared with experimental data. Phase selection rules based on different parameters were also investigated using both traditional methods and ML models.

2. Methods

2.1 CALPHAD calculations

A program is written to predict the phase equilibrium of the 1,761 SS alloys using TC-Python, a python language-based software development kit (SDK) that allows Thermo-Calc to perform high throughput calculations. The computation settings were: TCHEA4 database, only BCC and FCC phases were entered (explained in the Results section), and 1100 °C which is the temperature at which all high-throughput thin film libraries were made.

2.2 Parameters for phase selection

Eight parameters are selected for studying the phase selection rules among 2,436 alloys: the mixing entropy (ΔS_{mix}), the mixing enthalpy (ΔH_{mix}), atomic size difference (δ) [52], Ω that links mixing entropy, mixing enthalpy and melting temperature [32,53], valence electron concentration (VEC) [25,26], the FCC-BCC-index (FBI) [15], number of itinerant electrons (e/a) [25,54], and the difference in Pauling electronegativity $\Delta \chi$ [4,55]. These parameters are defined as followings.

$$\Delta S_{mix} = -R \sum_{i=1}^{N} c_i ln c_i , \qquad (1)$$

$$\Delta H_{mix} = \sum_{i=1, i\neq j}^{N} \Omega_{ij} c_i c_j , \qquad (2)$$

$$\delta = 100\sqrt{\sum_{i=1}^{n} c_i (1 - r_i/\bar{r})^2}$$
, (3)

$$\Omega = \frac{T_m \Delta S_{mix}}{|\Delta H_{mix}|},\tag{4}$$

$$VEC = \sum_{i} c_{i} VEC_{i} , \qquad (5)$$

$$FBI = \sum_{i} c_i \, \varphi_i \, , \tag{6}$$

$$e/a = \sum_{i=1}^{N} c_i (e/a)_i$$
, (7)

$$\Delta \chi = \sqrt{\sum_{i=1}^{N} c_i (\chi_i - \bar{\chi})^2} , \qquad (8)$$

where c_i , r_i , VEC_i , $(e/a)_i$, χ_i , $\bar{r}(=\sum_{i=1}^n c_i\,r_i)$, $\bar{\chi}(=\sum_{i=1}^n c_i\,\chi_i)$ are the mole fraction, atomic radius, valency electron concentration, number of itinerant electrons, electronegativity of element i, average atomic radius, average electronegativity of an alloy. N is the number of elements in an alloy system, and R is the gas constant. $\Omega_{ij}(=4\Delta H_{mix}^{AB})$ is the regular solution interaction parameter between elements i and j [56], and ΔH_{mix}^{AB} is the mixing enthalpy of A-B binary liquid alloys whose values can be found in Refs. [57,58]. $T_m = \sum_{i=1}^n c_i(T_m)_i$, where $(T_m)_i$ is the melting point of element i. Φ_i is +1 for element i with either the FCC or HCP crystal structure, and ϕ_i is -1 for elements i with the BCC crystal structure.

2.3 Machine learning

With these eight parameters as input features, four supervised ML algorithms, decision tree (DT), k-nearest neighbor (KNN), SVM, and ANN were employed to predict the phase formation of the HEAs. These four algorithms are implemented using the scikit-learn package, a machine learning library in python [59]. Each algorithm has different tuning parameters that are used to adjust the training model. Five-fold cross-validation (CV) was employed to judge the performance of predictions, which can avoid the overfitting and underfitting phenomena in ML. The dataset is split randomly into five disjoint subsets with nearly the same size. The models were trained with 4 subsets and tested 5 times with the remaining subset. The 5-fold CV accuracy is the average of the 5 test accuracies, which is called CV accuracy for simplicity throughout this article.

The DT model divides the data at each parent node into the left child node and the right child node in a binary tree [60,61]. Shannon's entropy $H(X_n) = \sum_k p_{nk} log(p_{nk})$ is employed, where X_n denotes the data and p_{nk} stands for the proportion of class k outcome in all outcomes at node n, to measure the impurity information at node n. The DT algorithm minimizes the function $G(Q_m,\theta) = \frac{n_{left}}{N_m} H\left(Q_{left}(\theta)\right) + \frac{n_{right}}{N_m} H\left(Q_{right}(\theta)\right)$, where Q_m , Q_{left} , and Q_{right} represent the data at node m, the left child of node m, and the right child of m, respectively. n_{left} and n_{right} are the number of samples in the left child and the right child of node m, respectively. N_m is the number of samples at node m and θ is a candidate split for the Q_m . This algorithm achieves most information gain at the best split θ^* that minimizes G. However, using DT can overfit the data by generating overly complex trees, resulting in failure of predictions. Therefore, two parameters, the min_samples_leaf (the minimal number of samples at a node) and max_depth (the maximal depth of a tree) were controlled during our ML to regularize the size of trees to avoid overfitting.

KNN utilizes a voting mechanism by k nearest neighbors to a query sample [62,63]. In this way, the query sample is assigned to the class with major votes among k nearest neighbors. When the weight of voting for every nearest neighbor is the same, then KNN uses a uniform weight. However, the voting weight is often different for every voter since the voting power of every voter is not same. The distance weights are proportional to the inverse of distance between training sample and query sample and are used here because the contributions of nearer neighbors are generally more than that of farer neighbors, which is based on the

calculation of the standard Euclidean distance [64], $d(p,q) = \sqrt{\sum_{i=1}^n (p_i - q_i)^2}$, where p is a training vector and q is the query vector. Not only does the weight of a neighbor matter, but also the number of participating nearest neighbors. Thus, it is meaningful to control the number of nearest neighbors for obtaining high CV accuracy, which can be adjusted by the parameter n neighbors.

The SVM model implements one-versus-one method for multi-class classification [65]. It is chosen with radical basis function $k(x_i,x_j)=e^{-\gamma|x_i-x_j|^2}$ as the kernel function, where x_i and x_j are the features of ith and jth samples, and γ is the kernel coefficient in this work. Γ is also an indicator of the degree of effect of a training sample on other samples. A sample with larger γ has lower influence on other samples. Another penalty parameter C is also critical to control the tradeoff between the overfitting and simplicity of the decision surface. A large C could increase misclassification of samples in the training process and cause underfitting, while a small C could improve the training accuracy but may lead to overfitting for the training samples. Hence the appropriate parameters γ and C of the SVM model should be determined to obtain reasonable train and test outcomes.

ANN simulates the decision-making process of human mind by constructing artificial neurons in the model [66,67], whose architecture is illustrated in **Fig. 1**. It usually contains an input layer of the exploring features that are fed into separate neurons, some hidden layers whose quantity and number of neurons are affected by the complexity of data and number of classes, an output layer including the classified outcomes in each neuron. The input features propagate forward to each neuron in each hidden layer with fitted weights, then the fitting values are transformed by an activation function. The rectified linear unit activation function was employed here. At each hidden layer, a bias is introduced and propagates with the transformed fitting values to the next layer together. The propagating process stops till it arrives at the final output layer. When number of neurons is too large or too small, it has a negative influence on predictions, thus we search out the best set by using three hidden layers with the number of neurons n_1 , n_2 , n_3 in each layer ranged from 5 to 50 with an interval 5 – there are 1,000 total combinations.

Since the effects of the initial 8 input features on phase prediction are likely very different, it is very valuable to perform a systematic screening of the features and find those that are more critical phase selection criteria. The forward selection is applied with a three-step procedure for each model [36,68–70]. First step is training these features separately and creating an initial empty feature pool. The feature with the highest CV accuracy is added to the initial pool of features. The second step is adding next feature that increases the CV accuracy most to the previous pool of features from remaining features until all the features are stored in the feature pool. Therefore, a pool of features is ranked by their importance to ML models in datasets. The last step is selecting a cutoff point from the ordered optimal pool for each ML model, where the increase in the CV accuracy by adding a new feature to the pool becomes smaller than the standard deviation of the CV accuracy.

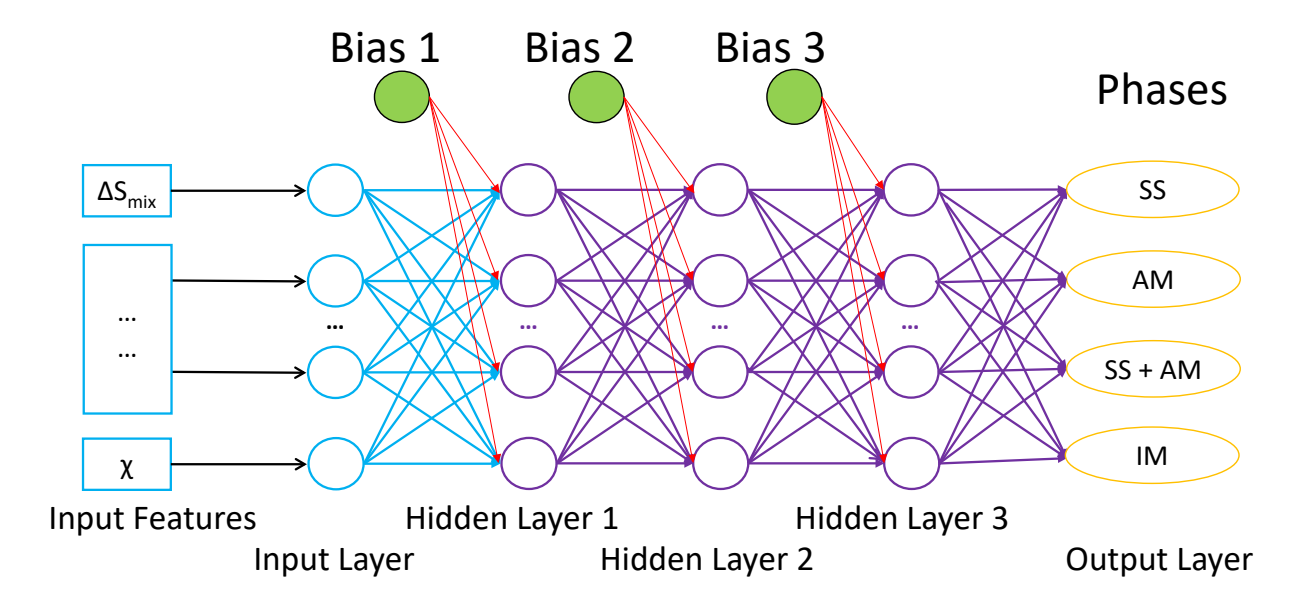


Fig. 1. The architecture of neural network with three hidden layers for classification (prediction) of SS, AM, SS + AM, and IM phases.

3. Results and Discussion

3.1. CALPHAD results

3.1.1 Comparison between experimental data and CALPHAD predictions

We first performed unconstrained high-throughput thermodynamic calculations of the equilibrium phases at the experimental temperature (1100 °C) for each of the 2,436 HEAs using the Thermo-Calc software and its associated TCHEA4 thermodynamic database, and the calculations are presented Figs. S1 and S2 in the Supplementary Information. The results are very different from the experimental observations reported by Kube et al., including the formation of IMs in far more alloys than experimental observations as well as the formation of liquid in a large number of alloys. Since the liquid phase was not observed during the experimental co-sputtering process of the combinatorial films, it is thus excluded in subsequent thermodynamic calculations in this study. The experimental IM consists of Sigma and other possible unidentified phases, which makes it hard to compare with thermodynamic calculations. However, we also tried to perform constrained calculations for the 233 alloys with the IM phase from experiments after excluding the liquid phase and it predicts 146 SS and 87 Sigma + SS alloys, which deviates significantly from the experimental observations, as shown in Fig. S3(a) and (b) in the Supplementary Information. The prediction of the IM formation is also beyond the capabilities of the current TCHEA4 database, similar to the situation in Ni-based superalloys [71], thus IMs are also excluded in further calculations; and we focused on calculating and analyzing the phase formation of the SS alloys.

Calculations using the TCHEA4 database predicted far more alloys with the B2 phase and B2 associated two-phase cases (B2+FCC and BCC+B2) as well as the BCC+B2+FCC threephase cases than the experimental observations, as shown in Fig. 2(a). Far few single-phase BCC alloys were predicted at the expense of forming the B2 phase in a very large number of allovs. The TCHEA4 database calculations predicted the number of single-phase FCC allovs close to experimental observations, but the overall consistency with experimental observations (including all the matched predictions of BCC, B2, BCC+FCC, and B2+FCC phases) is only 28.2%. When the single-phase B2 and single-phase BCC phases are regarded as one BCCbased single phase (BCC/B2), the agreement between the Thermo-Calc results and experimental observations is much better and reaches 61.4%, Fig. 2(b), showing less singlephase BCC/B2 and single-phase FCC, and more BCC/B2 + FCC two-phase cases. It is very likely that the Thermo-Calc database TCHEA4 does not have accurate enough thermodynamic parameters for the B2 phase whose Gibbs free energy is very close to the disordered BCC phase and thus hard to be modeled accurately, especially for multicomponent HEAs. The disparity between the CALPHAD predictions (representing the phases of bulk alloys) and the sputtering experimental data may also be the results of some non-equilibrium nature of the sputtering process [15].

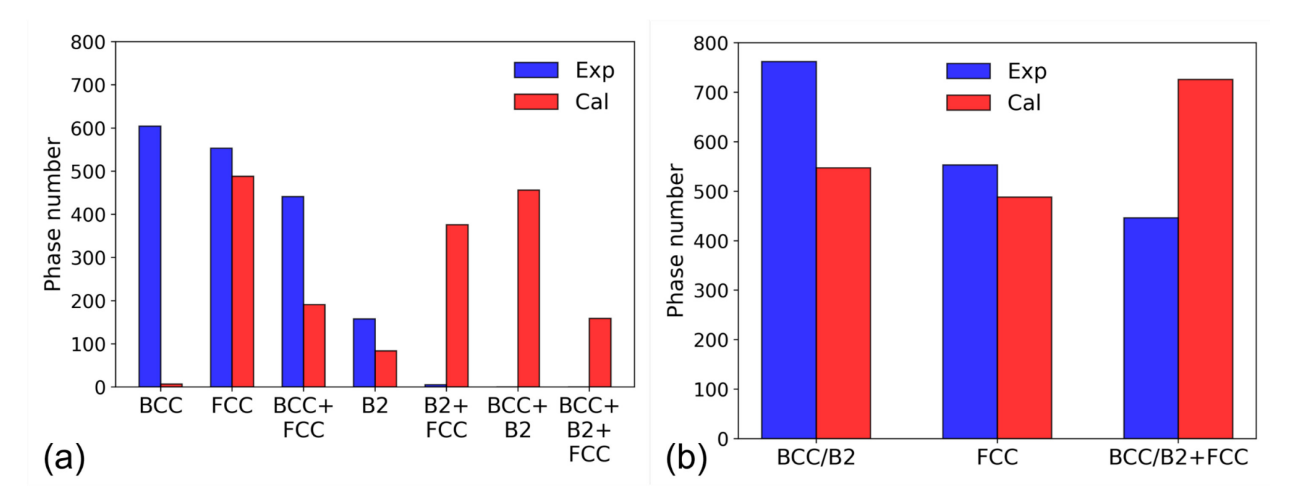


Fig. 2. Bar graphs showing the total number of HEAs with different phases: (a) B2 and BCC are treated as separate phases in CALPHAD calculations, and (b) B2 and BCC are treated as the same BCC-based phase (BCC/B2). The experimental data and CALPHAD predictions are presented in blue and red bars, respectively.

Fig. 3 compares the experimental observations in the left column (a) with the CALPHAD results in the middle column (b) by plotting the number of alloys in each category against VEC, showing again a higher number of the computed BCC/B2 + FCC two-phase alloys than experimental observations. The difference is also compared in **Fig. 3(c)**, the right column, where one can see that quite a number of the single-phase BCC/B2 alloys observed in experiments show up as the BCC/B2 + FCC two-phase alloys – the red part of the bottom panel of **Fig. 3(c)**. The red part of the top panel of **Fig. 3(c)** represents alloys that were observed as single-phase FCC experimentally but showed up as two-phase BCC/B2 + FCC in CALPHAD

calculations. Only a few alloys as represented by the blue part of the middle panel of **Fig. 3(c)** of the experimentally observed 2-phase (BCC/B2 + FCC) alloys were computed as single-phase BCC/B2. Similarly, the green part of the middle panel in **Fig. 3(c)** represents the experimentally observed 2-phase (BCC/B2 + FCC) alloys which were predicted to be single-phase FCC.

Fig. 3 also shows a clear trend that alloys with higher VEC prefer FCC over BCC/B2 both in experimental observations and CALPHAD predictions. A previous study has found that the FCC and BCC phases tend to be stable at higher VEC (> 8) and lower VEC (< 6.87), respectively [26]. The rule of VEC < 6.87 for single-phase BCC/B2 formation holds well with respect to the 1,761 SS HEAs, as shown in **Fig. 3**. The VEC > 8 rule also holds well for the formation of single-phase FCC, but at 8 < VEC < 9.16, there is also substantial alloys with BCC/B2 + FCC two-phase structure. Only when VEC > 9.16, the single-phase FCC is formed with only a few exceptions in the CALPHAD predictions. At VEC < 6.87 and VEC > 9.16, the predicted phase formation is in good agreement with experimental observations, which illustrates the good ability of CALPHAD in calculating phase equilibrium of HEAs, especially for single-phase solid solution SPSS. Yang et al. found that more than 90% compositions have single-phase BCC structures at 5.7 ≤ VEC ≤ 7.2, and it has pure FCC structure at VEC > 8.4 in Al-Co-Cr-Fe-Ni system by high-throughput calculations using CALPHAD [28]. The new rules revealed from this study and that of Kube et al. [15] should be more reliable due to the very large number of experimental HEAs that consist of more elements.

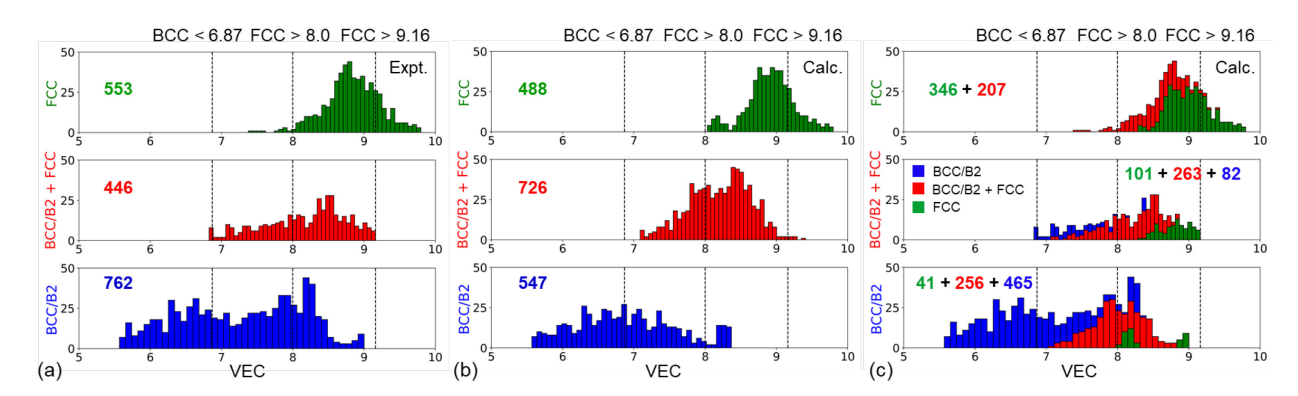


Fig. 3. VEC histograms based on experimental data in (a) and CALPHAD results in (b). (c) is plotted to show how alloys with different phases vary from experimental observations to the CALPHAD predictions.

3.1.2. VEC, FBI, ΔH_{mix} , Ω , and δ selection rules for SS alloys

The crystal structure, atomic radius, melting temperature, VEC, ϕ , e/a, and electronegativity of Al, Cr, Mn, Fe, Co, Ni, Cu in **Table 2** are used to calculate those aforementioned 8 parameters for HEAs [4]. Representative 2D plots are shown in **Fig. 4** in which the left-hand side and right-hand side columns plot the experimental results and the CALPHAD results, respectively, for comparison.

One can see from **Fig. 4(a)** and **4(b)** that at δ < 5 based the experimental data and δ < 4 based on the computed data, the FCC phase forms at higher FBI values, which is the direct consequence of the definition of FBI, Eq. 6. For experimental data at δ > 6, the FBI effect

breaks down and almost all alloys form single-phase BCC irrespective of the FBI values, showing the overwhelming effect of δ in dictating the formation of BCC when δ value is high. This phenomenon is also verified and is more obvious in the CALPHAD calculations. Formation of BCC/B2 over FCC with increasing size difference δ was attributable to the lower packing density of BCC/B2 and higher ability to accommodate atoms with different sizes than FCC structure [15].

Table 2. Crystal structure, atomic radius r, T_m , VEC, φ , e/a, χ of each element involved in this study (Data from Ref. [4]).

Element	Structure	r (Å)	T _m (K)	VEC	φ	e/a	χ
Al	FCC	1.4317	933	3	1	3	1.61
Cr	BCC	1.2491	2180	6	-1	1	1.66
Mn	Cubic	1.3500	1519	7	±0	2	1.55
Fe	BCC	1.2412	1811	8	-1	2	1.83
Co	HCP	1.2510	1768	9	1	2	1.88
Ni	FCC	1.2459	1728	10	1	2	1.91
Cu	FCC	1.2780	1358	11	1	1	1.90

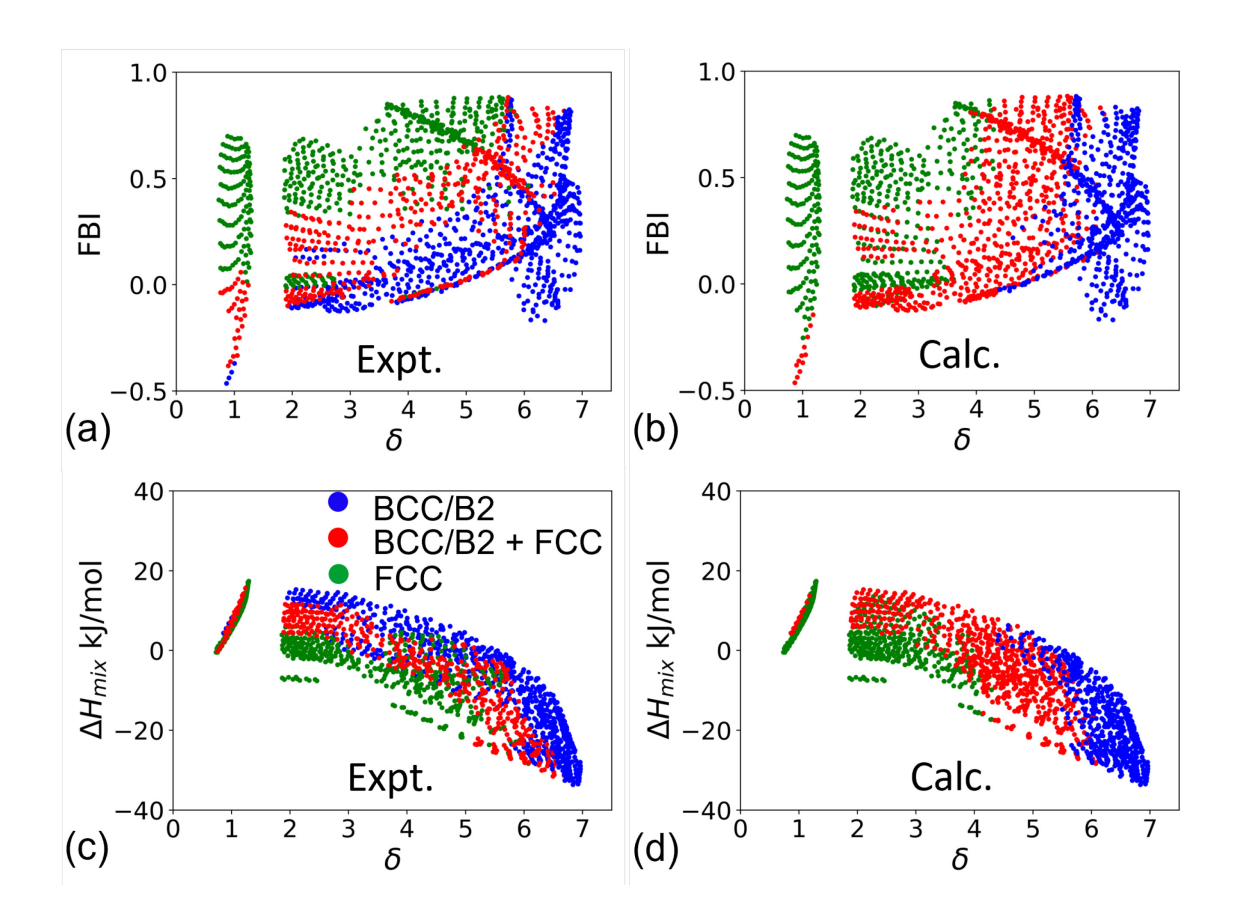


Fig. 4. FBI, ΔH_{mix} and Ω versus δ based on experimental data in (a) and (c); as well as CALPHAD predictions in (b) and (d).

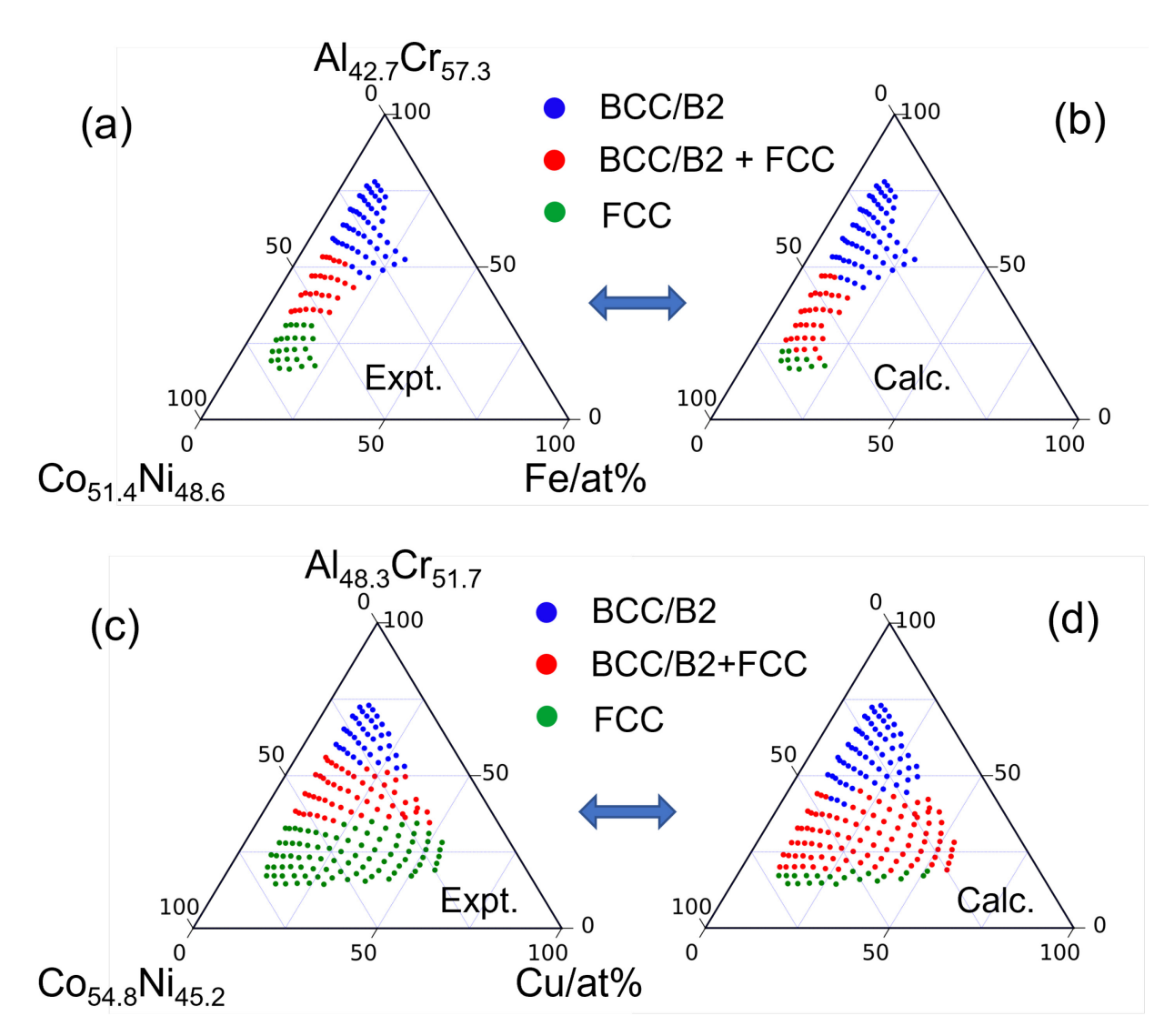


Fig. 5. Comparison of phase formation between experimental and computational (CALPHAD) results in the pseudo-ternary $Fe - Co_{51.4}Ni_{48.6} - Al_{42.7}Cr_{57.3}$ system shown in (a) and (b) as well as the pseudo-ternary $Cu - Co_{54.8}Ni_{45.2} - Al_{48.3}Cr_{51.7}$ system in (c) and (d).

Guo and Liu [29] found that ΔH_{mix} and δ for the formation of SS should satisfy $-22 \le \Delta H_{mix} \le 7$ kJ/mol, $0 \le \delta \le 8.5$, and $11 \le \Delta S_{mix} \le 8.5$ simultaneously. Our study, covering far more alloy compositions than those of Guo and Liu, shows that the ΔH_{mix} range for the formation of FCC is similar to that of Guo and Liu, but it can be expanded to -33.6kJ/mole to 17.5 kJ/mol for forming single-phase BCC/B2, **Fig. 4(c)** and **(d)**. Single-phase BCC can form at a negative ΔH_{mix} and larger δ values, which agrees with the work of Raghaven et al [72] and Agarwal and Rao [43].

Our results also agree with the observation of Agarwal and Rao that BCC can coexist with FCC at a lower δ and FCC preferentially forms at a negative ΔH_{mix} while BCC prefer to form at a positive ΔH_{mix} . The CALPHAD results show similar trend but more pronounced separations of the phase formation regions, **Fig. 4(d)**. These phase selection rules are useful for predicting alloy crystal structures and compositions, but more effective rules are still highly desired; thus we will subsequently explore the capabilities of ML in improving the phase predictions.

3.1.3 Examples of phase formation in specific systems

Different HEA libraries cover different regions of the multicomponent HEA composition space. The agreements between experimental and computational results can be very different. Two examples are shown in **Fig. 5** to illustrate the degree of agreements for both the Al-Cr-Co-Ni-Fe and Al-Cr-Co-Ni-Cu systems. **Fig. 5(a)** and **(b)** show that for the compositions covered by a pseudo-ternary Fe - Co_{51.4}Ni_{48.6} - Al_{42.7}Cr_{57.3} system, the agreement is good except for a smaller single-phase FCC region and slightly larger BCC/B2 + FCC two-phase region from CALPHAD. Much pronounced difference was observed in **Fig. 5(c)** and **(d)** for the compositions covered by the pseudo-ternary Cu - Co_{54.8}Ni_{45.2} - Al_{48.3}Cr_{51.7} system. Such comparisons may also help identify the specific systems where CALPHAD assessments need to be improved.

3.2 Machine learning results

Two groups of datasets are analyzed using ML, one is the SS only dataset with 1,761 HEAs, the other is the full dataset with 2,436 HEAs. Similar to the analysis using CALPHAD, the SS is divided into three categories, BCC/B2, BCC/B2 + FCC, FCC, which are the targets of the ML models. The predictions from ML in the SS dataset are further compared with the experimental observations. The full dataset is classified into four classes, SS, AM, SS + AM, and IM as the output of the ML models. It is noted that IM is used here to refer to alloys with an intermetallic compound (mostly the σ phase) identified from XRD and some alloys contain additional phases in addition to IM. The ML models are optimized by adjusting their parameters first. Then the best feature sets are screened by their contributions towards improving the CV accuracy of predictions for each ML model, which provides information for the relative importance among these input features.

3.2.1 ML for classifying BCC/B2, BCC/B2 + FCC, FCC phases

Before training the ML model and making predictions, it is important to look into the correlation among these features because adding collinear features will not provide more valuable information and will increase the time cost of training and could even degrade the performance of the models. The Pearson correlation coefficient is used for the quantitative assessment of the correlation between any pair of features, and it is calculated with the following formula,

$$r_{xy} = \frac{\sum_{i=1}^{n} (x_i - \overline{x})(y_i - \overline{y})}{\sqrt{\sum_{i=1}^{n} (x_i - \overline{x})^2} \sqrt{\sum_{i=1}^{n} (y_i - \overline{y})^2}}$$

where x, y are the two variables/features, x_i and y_i are the x and y values of ith sample, \bar{x} and \bar{y} are the mean values of x and y, and y is the sample size of both x and y [73]. Using this formula, the correlation between any pair of features is shown in **Fig. 6**, indicating that all input

features can be kept and further used in the ML models since there is no high correlation coefficient between any two features.

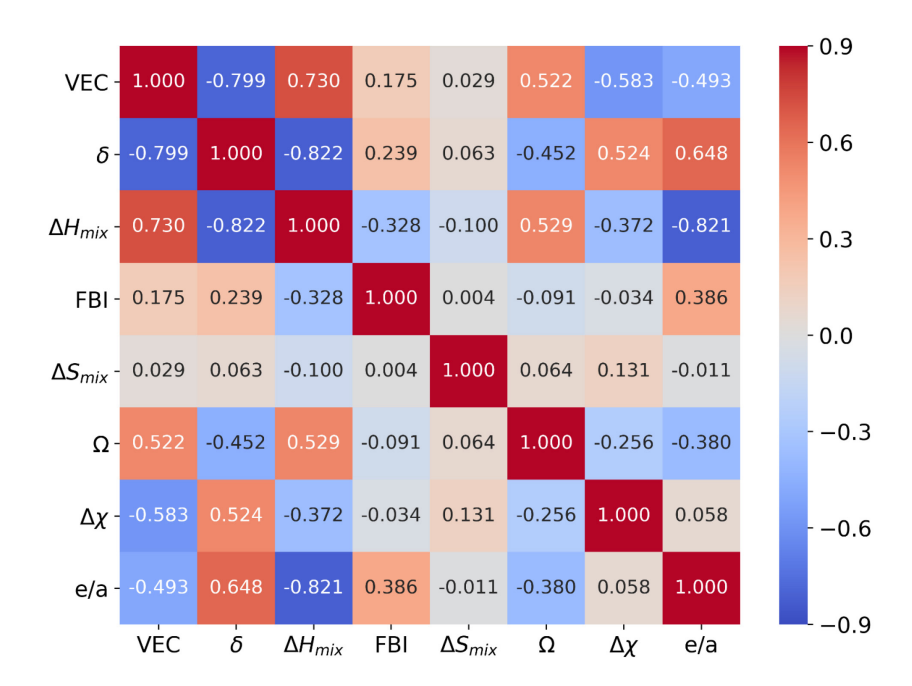


Fig. 6. The heat-map of the correlation matrix between any pair of features. The value at each cell is the calculated coefficient.

The ML models can be modified by tuning parameters and then judged by the CV accuracy. Here, the grid search method was employed to adjust parameters for each model with all the eight features, and the optimized results are shown in Fig. 7. The max depth is identified as the main factor in determining the quality of the DT model and the min samples leaf has negligible effect, Fig. 7(a). The CV accuracy of the DT model reaches highest when max depth is 10 and stay stable after 10; thus min samples leaf = 2 and max depth = 10 were selected for the final DT model. The n neighbors = 2 is best for the KNN model in Fig. 7(b). For SVM, a parameter set of $\gamma = 10^p$ and $C = 2^q$ is created, where $-6 \le p \le 4$ and $1 \le q \le 10$. Both γ and C affect the accuracy of the SVM model, and both cannot be too large or too small; otherwise, they would lead to inefficiency. The pair of $\gamma = 0.01$ and C = 64 (p = -2, q = 6) achieved a high CV accuracy from the parameter sets, Fig. 7(c). The neural network was built with three hidden layers that contain n₁, n₂, n₃ neurons in each hidden layer, and the corresponding CV result is shown in Fig. 7(d). For each third hidden layer with neurons changing from 5 to 50 (interval 5), the combination of three layers' neurons with highest CV accuracy is marked in black dot, so there are 10 highest CV accuracies shown in 10 black dots. Finally, the combination $n_1 = 35$, $n_2 = 25$, $n_3 = 10$ is chosen from these 10 CV accuracies.

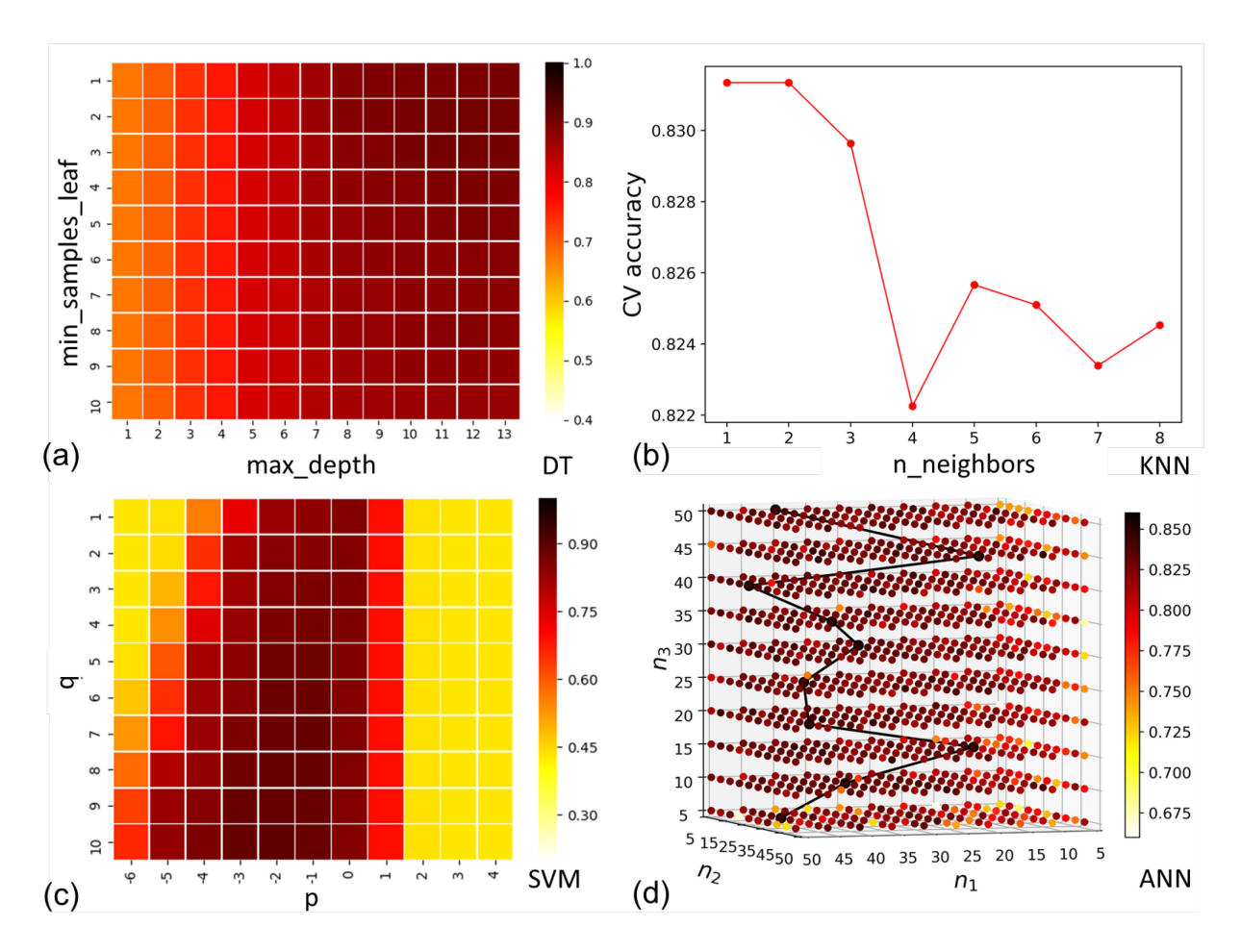


Fig. 7. The grid search method for tuning input parameters to obtain the high CV accuracy in each ML model: (a) DT, (b) KNN, (c) SVM, (d) ANN, respectively.

The results of feature selections for the four ML models are shown in **Fig. 8**. The CV accuracy increases rapidly first, then stays stable, and finally decreases when more input features are employed for the ML models, **Fig. 8(a)**, indicating that more features are not always helpful in ML because they could lead to overfitting in the training process and decreasing CV test accuracy. The order of precedence of the features in each ML model are shown in **Fig. 8(b)**, and the best feature sets for different ML models are colored for easier visualization. The {VEC, ΔH_{mix} , e/a, δ } set is the best features for the DT model, which renders a 91.4% CV accuracy. Adding other features does not improve the performance of learning. The {VEC, δ , FBI, e/a}, and { VEC, ΔH_{mix} , e/a, δ , ΔS_{mix} }, {VEC, ΔH_{mix} , e/a, δ , ΔS_{mix} } sets are the best three feature combinations for KNN, SVM, and ANN, which achieves 93.1%, 90.2%, and 89.1% CV accuracy, respectively. In all four feature sets, the VEC feature owns the highest order of precedence, thus is the most influential among these eight features in determining SS formation. It is noted that the CV accuracy obtained by using only VEC feature is comparable to or even better than the prediction accuracy from CALPHAD; and the CV accuracy is higher than

85% after training with the first three best features in each ML model, showing advantages of phase predictions over current state of thermodynamic calculations. The other features that are helpful for enhancing prediction accuracies are ΔH_{mix} , e/a, δ . The two worst features are Ω and Δχ that degrade the performance of the ML models in predicting SS formation. Li and Guo also found that VEC is the most important feature in classifying BCC, FCC, and NSP (not forming SPSS) with the SVM model and the CV accuracy reaches 90.7% under the input of {VEC, δ, T_m, ΔH_{mix} , ΔS_{mix} feature set [68]. A study by Zeng et al. explored >300,000 phase equilibrium generated by CALPHAD calculations in 3 classes (single-phase FCC, single-phase BCC, and other phases) using XGBoost [48]. They achieved > 99% accuracy on both the training set and the test set and predicted 155 experimental phases with 81% accuracy through the selection of 5 most important features {equilibrium temperature, average atomic radius, VEC difference, VEC, $\Delta \chi$. A feature set of 13 top-ranked features was screened in classifying BCC, FCC, and BCC + FCC by Machaka, and VEC was found to have the highest relative importance [49]. His models can reach 97.5%, 95.8%, 94.35%, and 94.0% using random forest (RF), SVM, KNN, and ANN, which is slightly higher than the current study possibly due to the larger set of features used in his study. Zhang et al. utilized a genetic algorithm with ANN and also found that the VEC criterion is important in classifying BCC, FCC, and dual-phase HEAs [70]. Their classification accuracy achieved 91.3% with a feature set containing VEC, the core electron distance, $\Delta \chi$, the mismatch in compression modulus. Their CV accuracy is comparable to ours in ANN learning. Overall, the accuracy could reach higher than 89% for these four models, making the application of ML in phase prediction significant.

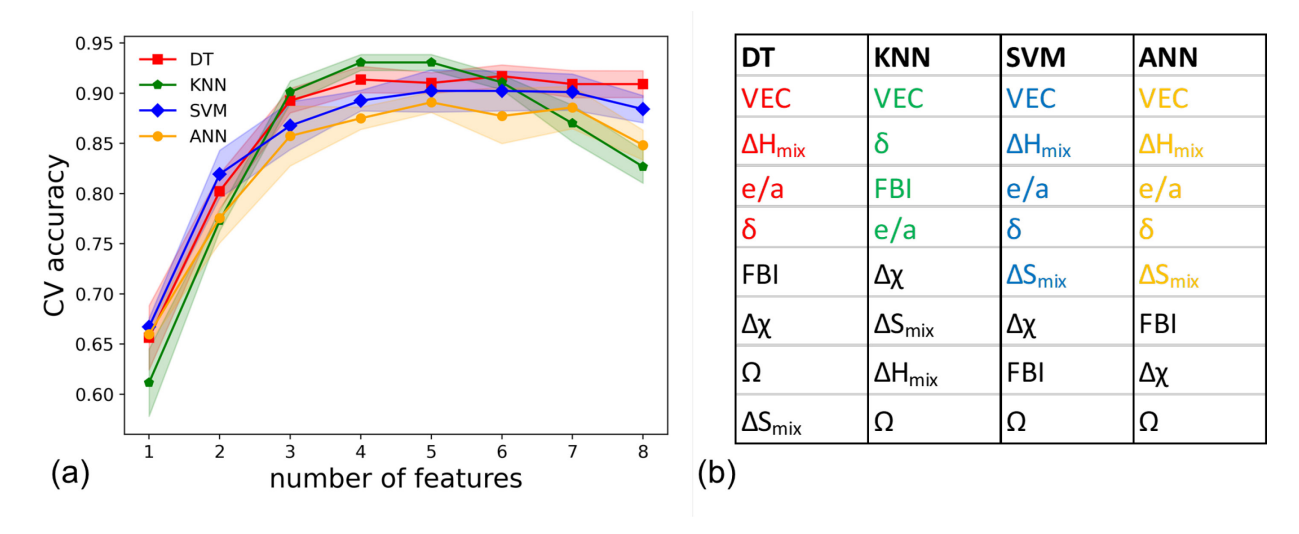


Fig. 8. (a) Feature selection process to increase the CV accuracy in each ML model for classifying the BCC/B2, BCC/B2 + FCC, FCC phases of the solid-solution only compositions. (b) Corresponding features based on the order of precedence from top to bottom after each selection step. The colored features are the best sets that achieve the performance of the ML models.

Since ML has found both VEC and ΔH_{mix} are the two most significant features to predict the SS phases, VEC-vs- ΔH_{mix} plots are made based on experimental results in **Fig. 9(a)** and SVM

ML predictions in **Fig. 9(b)**. All alloys with BCC/B2 + FCC two phases are located in the shading red region in **Fig. 9(a)**. Towards the left side of this region is single-phase BCC/B2 and single-phase FCC on the right side. By counting the correct phases predicted by this division strategy, the accuracy is 67.1% in **Fig. 9(a)**, which is much more efficient than relying on the VEC only (VEC < 6.87 for BCC/B2 and VEC > 9.16 for FCC). The colored areas in **Fig. 9(b)** are the predicted phases by SVM, and the boundaries for classification are curves rather than straight lines. When experimental data points are in the area with same color, then the predictions for phases agree with experiments (Note some of the red color points are outside the red region). The CV accuracy achieves 81.9% by SVM based on VEC and ΔH_{mix} , exhibiting the advantages of ML in predicting right phases over traditional strategies. We also used the ML models to study the classification on BCC, B2, FCC, BCC + FCC, and B2 + FCC phases (having B2 and BCC separately) and found that VEC is still the most important feature in every ML model as shown in **Fig. S6** in the Supplementary Information.

The VEC-vs- ΔH_{mix} plots are far more accurate in predicting the single-phase BCC/B2 and single-phase FCC solid solutions without considering the BCC/B2 + FCC two-phase alloys, as shown in **Fig. 9(c)** and **(d)**. Even a simple plot of experimental data only, a simple straight line of $\Delta H_{mix} = 28.97 \times VEC - 246.77$ can achieve 96.2% accuracy, which is simply remarkable, **Fig. 9(c)**. The CV accuracy of 96.4%, 97.0%, 97.4%, and 96.5% is achieved for DT, KNN, SVM, and ANN, respectively, not significantly better than the predicted results determined by the straight line, **Fig. 9(d)** which shows SVM results only. Even though the simply plots of experimental data achieve excellent abilities to predict the right phases, it is ML that helps identify these two key parameters for the plots.

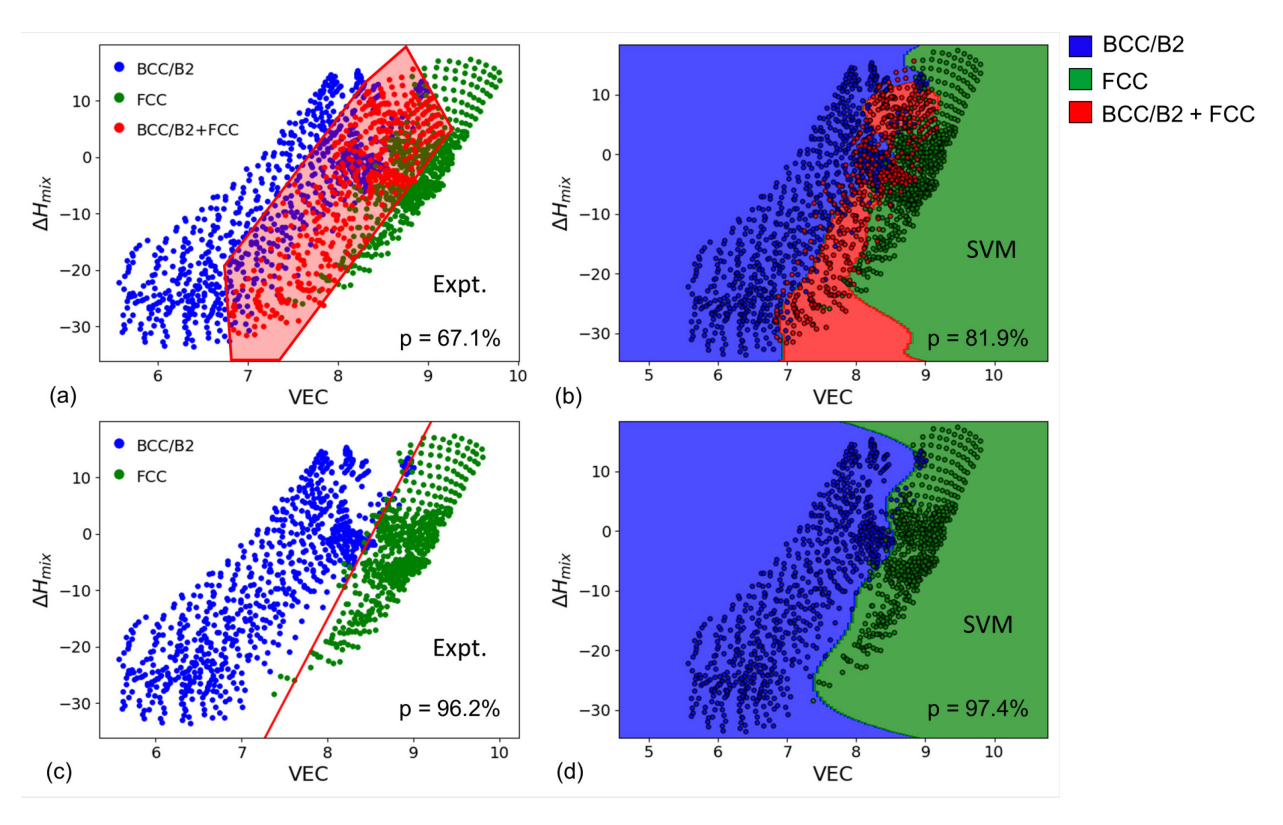
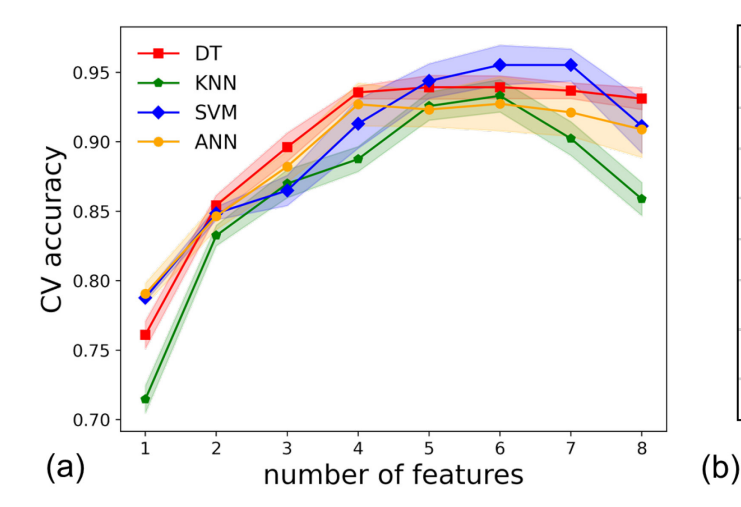


Fig. 9. VEC vs ΔH_{mix} plots for SS data in (a) and (b), and SPSS data in (c) and (d), respectively. The experimental data are plotted in circle points and predictions by SVM are plotted in colored area in (b) and (d), where the blue, red, and green area manifests predicted BCC/B2, BCC/B2 + FCC, and FCC phases, respectively. The p value refers to the prediction accuracy in (a) and (c), and the CV accuracy in (b) and (d).

With these well-trained models, we applied them to predict the selected alloy systems (containing 13 elements) that were tested in the study of Zeng et al. [49]. The compositions, experimentally determined phases, and ML-predicted phases are shown in the Supplementary Information **Table S1**. ANN beats other ML models with highest overall prediction accuracy 81.8%, demonstrating the feasibility of using trained ANN with thin-film data to predict the phase formation of bulk alloys. The CALPHAD prediction accuracy is 78.8% without a constrained limit and 86.4% with constrained input of only BCC and FCC phases. The prediction accuracy of ANN lies in between the two CALPHAD predictions, exhibiting a comparable prediction ability of ANN with CALPHAD. There is an advantage of using ANN over CALPHAD in predicting the phase equilibria of bulk alloys whose elements are not available in the TCHEA4 or other HEA CALPHAD database.

3.2.2 ML for classification of SS, AM, SS + AM, and IM phases

In addition to analyzing the classification of SS into BCC/B2, BCC/B2 + FCC, and FCC, ML was applied to distinguish SS from other phases, such as AM, SS + AM, and IM. Such information is very beneficial for the design of new materials, especially when it is necessary to avoid the additional phases. The ML process of tuning parameters for SS, AM, SS + AM, IM phases are the same as that for the SS process in the above discussions and the corresponding plots are presented in **Fig. S4** in the Supplementary Information. The best conditions are min_samples_leaf = 2 and max_depth = 10 for the DT model, n_neighbors = 4 for KNN, γ = 0.01 and C = 256 for SVM, and n_1 = 50, n_2 = 15, n_3 = 35 for ANN. The feature selection process and the corresponding CV accuracy values are shown in **Fig. 10**.



DT	KNN	SVM	ANN
Δχ	Δχ	Δχ	Δχ
FBI	FBI	FBI	FBI
ΔH_{mix}	e/a	ΔH_{mix}	ΔH_{mix}
VEC	VEC	VEC	δ
δ	δ	δ	e/a
Ω	ΔS_{mix}	ΔS_{mix}	VEC
ΔS _{mix} e/a	ΔH_{mix}	e/a	ΔS_{mix}
e/a	Ω	Ω	Ω

Fig. 10. (a) Feature selection process measured by the CV accuracy in each ML model for predicting SS, AM, SS+AM, and IM. (b) Corresponding features based on the order of

precedence from top to bottom after each selection step. The colored features are the best sets that achieve the performance of the ML models.

The best four feature sets are $\{\Delta \chi$, FBI, ΔH_{mix} , VEC $\}$, $\{\Delta \chi$, FBI, e/a, VEC, δ , $\Delta S_{mix}\}$, $\{\Delta \chi$, FBI, ΔH_{mix} , VEC, δ , ΔS_{mix} }, { $\Delta \chi$, FBI, ΔH_{mix} , δ } with a CV accuracy of 93.6%, 93.3%, 95.5%, 92.7% for DT, KNN, SVM, ANN, respectively. The CV accuracies of these ML models are very high and very close to one another. The two best features for predicting the phases here are $\Delta \chi$ and FBI, which is different with VEC as the best feature in classifying BCC/B2, BCC/B2 + FCC, and FCC phases. Islam et al. found that VEC and ΔS_{mix} are the most and the least important features respectively in classifying AM, SS, and IM, by performing singular value decomposition on the weight matrix in the first hidden layer of ANN [39]. Our results also show the positive effect of VEC in helping classify phases, but it is not the most important feature. The VEC feature has the fourth priority in the feature set of DT, KNN, and SVM. It can also be seen that Ω is not helpful in predictions in both the full dataset and SS dataset from Fig. 10(b) since it decreases the CV accuracy when it is added into the input features. To separate SS and IM, King et al. proposed a new parameter Φ related to mixing enthalpy of both SS and IM by means of Miedema's model [74]. They found that $\Phi > 1$ favors SS and almost all IM forms when $\Phi < 1$, which forecasts more accurately than using Ω . Zhou et al. reported that their trained ANN, convolutional neural network (CNN), and SVM can reach around 95% accuracy with 13 features and reach around 89% with 4 features $\{\Delta S_{mix}, \delta, \Delta H_{mix}, \Delta \chi\}$ in predicting AM, IM, and SS. The 4 top-ranked features they selected are amongst our selected feature sets. The CV accuracy with only $\Delta \chi$ and FBI as the two input features can reach more than 80% for the four ML models, which motivates us explore the $\Delta \chi$ -vs-FBI plot as a potential useful phase selection rule.

In the $\Delta\chi$ -vs-FBI plot shown in **Fig. 11**, all amorphous alloys are in the purple shading area, where $-0.065 \le \text{FBI} \le 0.5$ and $0.13 \le \Delta\chi \le 0.165$. All intermetallics with only one exception are in the black shading area, in which FBI ≤ 0.015 and $\Delta\chi \ge 0.09$. These two shading areas only have a small, overlapped area of which the most SS alloys form in the lower right area. Therefore, these two areas could be used as phase selection rules for screening amorphous alloys and intermetallics, respectively. The ML methods are also applied to classify BCC, B2, FCC, BCC+FCC, B2+FCC, BCC+AM, FCC+AM, BCC+FCC+AM, AM, and IM phases (having B2 and BCC separately) and FBI and δ are found to be the two best features in improving the CV accuracies rather than $\Delta\chi$ and FBI as shown in **Fig. S8**. The corresponding FBI-vs- δ plot is shown in **Fig. S9** in the Supplementary Information.

4. Conclusions

High-throughput CALPHAD calculations were performed on 2,436 experimental HEAs and compared the results with experimental observations. Both CALPHAD predictions and experimental results show that alloys prefer BCC/B2 over FCC at larger atomic size difference which is understandable since BCC is less constrained than FCC, and alloys tend to form FCC structure at higher FBI, negative ΔH_{mix} , and small δ . Alloys exhibit single-phase BCC/B2 at VEC

< 6.87 and FCC at VEC > 9.16, which agrees with prior findings for BCC/B2, but the range has been expanded beyond VEC > 8 for FCC as reported in the literature.

Four ML models were applied to two different datasets, one with the 1,761 solid solution only HEA compositions and the other with the entire 2,436 HEAs with alloys with form amorphous (AM) and/or intermetallic compounds (IMs). The best feature sets were identified using the five-fold cross validation method and achieve 91.4%, 93.1%, 90.2%, 89.1% for classifying BCC/B2, BCC/B2 + FCC, FCC with DT, KNN, SVM, and ANN models, respectively. These trained models were applied on predicting the phase structures of 66 selected bulk alloys, and the ANN model achieved 81.8% prediction accuracy, which is comparable to CALPHAD predictions. For classification of SS, AM, SS + AM, IM phases, the CV accuracy can reach 93.6%, 93.3%, 95.5%, and 92.7% in DT, KNN, SVM, and ANN models, respectively. The CV accuracies for both datasets are very high, which shows the effectiveness of ML in phase predictions of HEAs. In the ranked feature sets, VEC is identified as the most important feature in determining phase formation of SS. ML identified both ΔH_{mix} and VEC as two dominating factors for predicting the solid solution phase; and based on this learning, a simple straight line of $\Delta H_{mix} = 28.97 \times VEC - 246.77$ was found to be able to predict single-phase BCC/B2 and single-phase FCC at 96.2% accuracy, which is simply remarkable, **Fig. 8(c)**.

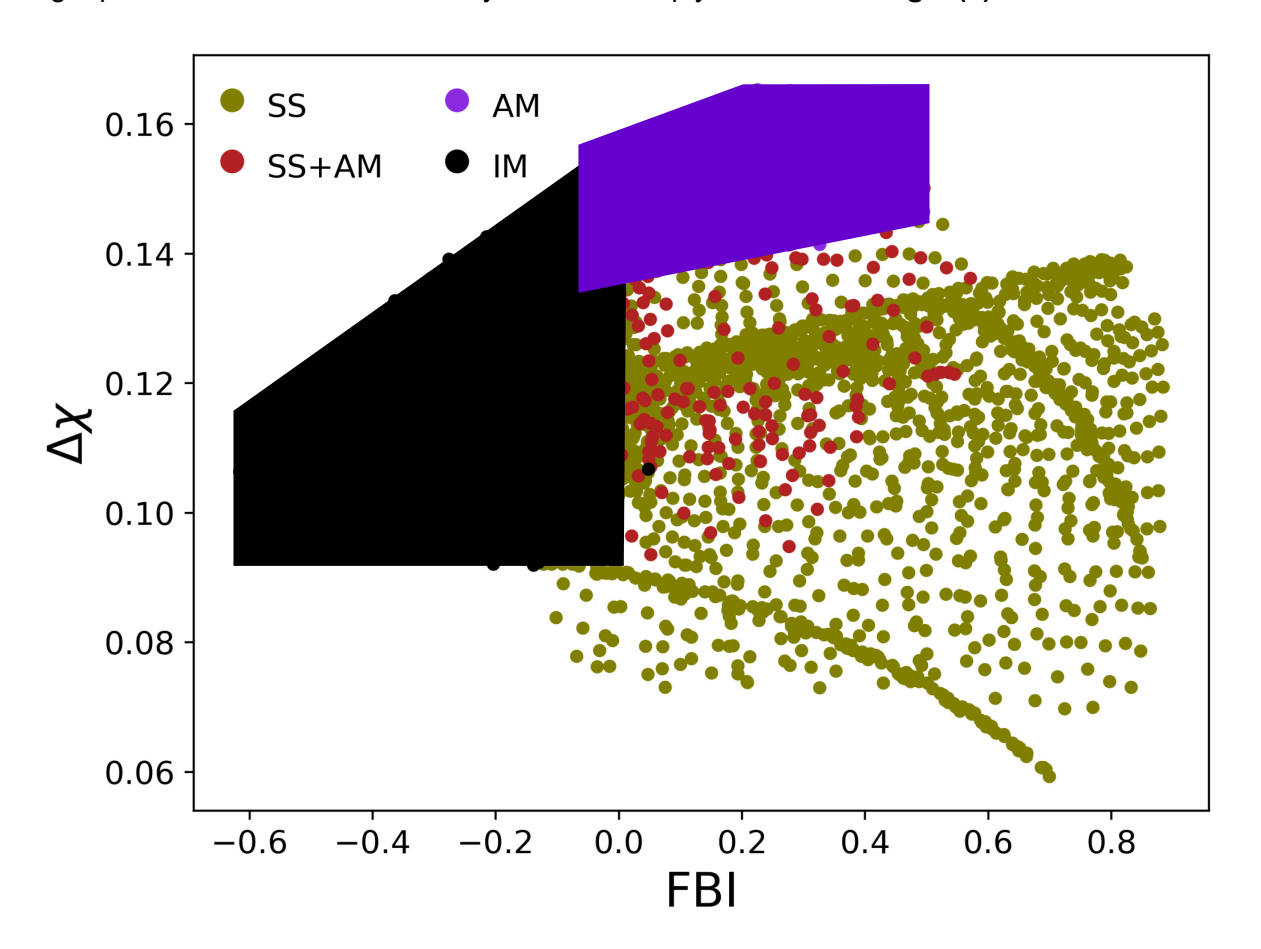


Fig. 11. FBI-vs- $\Delta \chi$ plot for identification of SS, AM, SS+AM, and IM. Most IM-containing alloys are in the black shading area in the left-hand side with only one exception.

Both $\Delta\chi$ and FBI are the two best features that improve the performance of ML models in predicting the formation of SS, AM, SS + AM, and IM phases. In the $\Delta\chi$ -vs-FBI plot shown in **Fig. 10**, all amorphous alloys are in the purple shading area, where $-0.065 \le FBI \le 0.5$ and $0.13 \le \Delta\chi \le 0.165$. All intermetallic-containing alloys with only one exception are in the black shading area, in which FBI ≤ 0.015 and $\Delta\chi \ge 0.09$. All these phase selection rules will be very valuable for future design of advanced HEAs for challenging applications.

Conflicts of interest

The authors declare no competing financial interests.

Funding

The thermodynamic and ML analyses performed at University of Maryland was funded by the U.S. National Science Foundation (NSF) Division of Civil, Mechanical and Manufacturing Innovation (CMMI) through award #2004979.

References

- [1] J.W. Yeh, S.K. Chen, S.J. Lin, J.Y. Gan, T.S. Chin, T.T. Shun, C.H. Tsau, S.Y. Chang, Nanostructured high-entropy alloys with multiple principal elements: Novel alloy design concepts and outcomes, Adv. Eng. Mater. 6 (2004) 299–303. https://doi.org/10.1002/adem.200300567.
- [2] M.H. Tsai, J.W. Yeh, High-entropy alloys: A critical review, Mater. Res. Lett. 2 (2014) 107–123. https://doi.org/10.1080/21663831.2014.912690.
- [3] U.L. Ganesh, H. Raghavendra, Review on the transition from conventional to multi-component-based nano-high-entropy alloys—NHEAs, J. Therm. Anal. Calorim. 139 (2020) 207–216. https://doi.org/10.1007/s10973-019-08360-z.
- [4] D.B. Miracle, O.N. Senkov, A critical review of high entropy alloys and related concepts, Acta Mater. 122 (2017) 448–511. https://doi.org/10.1016/j.actamat.2016.08.081.
- [5] A.D. Pogrebnjak, İ. V. Yakushchenko, A.A. Bagdasaryan, O. V. Bondar, R. Krause-Rehberg, G. Abadias, P. Chartier, K. Oyoshi, Y. Takeda, V.M. Beresnev, O. V. Sobol, Microstructure, physical and chemical properties of nanostructured (Ti-Hf-Zr-V-Nb)N coatings under different deposition conditions, Mater. Chem. Phys. 147 (2014) 1079–1091. https://doi.org/10.1016/j.matchemphys.2014.06.062.
- [6] J.M. Rickman, H.M. Chan, M.P. Harmer, J.A. Smeltzer, C.J. Marvel, A. Roy, G. Balasubramanian, Materials informatics for the screening of multi-principal elements and high-entropy alloys, Nat. Commun. 10 (2019) 1–10. https://doi.org/10.1038/s41467-019-10533-1.
- [7] B. Gludovatz, A. Hohenwarter, D. Catoor, E.H. Chang, E.P. George, R.O. Ritchie, A fracture-resistant high-entropy alloy for cryogenic applications, Science (80-.). 345 (2014) 1153–1158. https://doi.org/10.1126/science.1254581.
- [8] Y. Lu, Y. Dong, S. Guo, L. Jiang, H. Kang, T. Wang, B. Wen, Z. Wang, J. Jie, Z. Cao, H. Ruan, T. Li, A promising new class of high-temperature alloys: Eutectic high-entropy alloys, Sci. Rep. 4

- (2014) 1-5. https://doi.org/10.1038/srep06200.
- [9] C.M. Lin, H.L. Tsai, Evolution of microstructure, hardness, and corrosion properties of highentropy Al_{0.5}CoCrFeNi alloy, Intermetallics. 19 (2011) 288–294. https://doi.org/10.1016/j.intermet.2010.10.008.
- [10] Y. Zhang, T. Ting, Z. Tang, M.C. Gao, K.A. Dahmen, P.K. Liaw, Z. Ping, Microstructures and properties of high-entropy alloys, Prog. Mater. Sci. 61 (2014) 1–93. https://doi.org/10.1016/j.pmatsci.2013.10.001.
- [11] L.S. Zhang, G.L. Ma, L.C. Fu, J.Y. Tian, Recent progress in high-entropy alloys, Adv. Mater. Res. 631 (2013) 227–232. https://doi.org/10.4028/www.scientific.net/AMR.631-632.227.
- [12] O.N. Senkov, S. V. Senkova, C. Woodward, D.B. Miracle, Low-density, refractory multi-principal element alloys of the Cr-Nb-Ti-V-Zr system: Microstructure and phase analysis, Acta Mater. 61 (2013) 1545–1557. https://doi.org/10.1016/j.actamat.2012.11.032.
- [13] K.M. Youssef, A.J. Zaddach, C. Niu, D.L. Irving, C.C. Koch, A novel low-density, high-hardness, high-entropy alloy with close-packed single-phase nanocrystalline structures, Mater. Res. Lett. 3 (2014) 95–99. https://doi.org/10.1080/21663831.2014.985855.
- [14] Y. Li, K.E. Jensen, Y. Liu, J. Liu, P. Gong, B.E. Scanley, C.C. Broadbridge, J. Schroers, Combinatorial strategies for synthesis and characterization of alloy microstructures over large compositional ranges, ACS Comb. Sci. 18 (2016) 630–637. https://doi.org/10.1021/acscombsci.6b00040.
- [15] S.A. Kube, S. Sohn, D. Uhl, A. Datye, A. Mehta, J. Schroers, Phase selection motifs in High Entropy Alloys revealed through combinatorial methods: Large atomic size difference favors BCC over FCC, Acta Mater. 166 (2019) 677–686. https://doi.org/10.1016/j.actamat.2019.01.023.
- [16] A. Manzoni, H. Daoud, S. Mondal, S. Van Smaalen, R. Völkl, U. Glatzel, N. Wanderka, Investigation of phases in Al23Co15Cr23Cu8Fe15Ni16 and Al8Co17Cr17Cu8Fe17Ni33 high entropy alloys and comparison with equili, J. Alloys Compd. 552 (2013) 430–436. https://doi.org/10.1016/j.jallcom.2012.11.074.
- [17] H. Mao, H.L. Chen, Q. Chen, TCHEA1: A thermodynamic database not limited for "high entropy" alloys, J. Phase Equilibria Diffus. 38 (2017) 353–368. https://doi.org/10.1007/s11669-017-0570-7.
- [18] C. Zhang, F. Zhang, S. Chen, W. Cao, Computational thermodynamics aided high-entropy alloy design, Jom. 64 (2012) 839–845. https://doi.org/10.1007/s11837-012-0365-6.
- [19] T.M. Butler, M.L. Weaver, Investigation of the phase stabilities in AlNiCoCrFe high entropy alloys, J. Alloys Compd. 691 (2017) 119–129. https://doi.org/10.1016/j.jallcom.2016.08.121.
- [20] H.L. Chen, H. Mao, Q. Chen, Database development and Calphad calculations for high entropy alloys: Challenges, strategies, and tips, Mater. Chem. Phys. 210 (2018) 279–290. https://doi.org/10.1016/j.matchemphys.2017.07.082.
- [21] J.E. Saal, I.S. Berglund, J.T. Sebastian, P.K. Liaw, G.B. Olson, Equilibrium high entropy alloy phase stability from experiments and thermodynamic modeling, Scr. Mater. 146 (2018) 5–8. https://doi.org/10.1016/j.scriptamat.2017.10.027.
- [22] A. Karati, K. Guruvidyathri, V.S. Hariharan, B.S. Murty, Thermal stability of AlCoFeMnNi high-entropy alloy, Scr. Mater. 162 (2019) 465–467. https://doi.org/10.1016/j.scriptamat.2018.12.017.
- [23] R. Feng, C. Zhang, M.C. Gao, Z. Pei, F. Zhang, Y. Chen, D. Ma, K. An, J.D. Poplawsky, L. Ouyang, Y. Ren, J.A. Hawk, M. Widom, P.K. Liaw, High-throughput design of high-performance lightweight high-entropy alloys, Nat. Commun. 12 (2021) 6–15. https://doi.org/10.1038/s41467-021-24523-9.
- [24] U.R. Kattner, The thermodynamic modeling of multicomponent phase equilibria, Jom. 49 (1997) 14–19. https://doi.org/10.1007/s11837-997-0024-5.
- [25] U. Mizutani, The Hume-Rothery rules for structurally complex alloy phases, Surf. Prop. Eng. Complex Intermet. (2010) 323–399.
- [26] S. Guo, C. Ng, J. Lu, C.T. Liu, Effect of valence electron concentration on stability of fcc or bcc phase in high entropy alloys, J. Appl. Phys. 109 (2011) 103505. https://doi.org/10.1063/1.3587228.
- [27] L. Jiang, Verification and Optimization of Single Phase Solid Solution Rule in High Entropy Alloys, Jom. 72 (2020) 2949–2956. https://doi.org/10.1007/s11837-019-03977-9.
- [28] S. Yang, J. Lu, F. Xing, L. Zhang, Y. Zhong, Revisit the VEC rule in high entropy alloys (HEAs)

- with high-throughput CALPHAD approach and its applications for material design-A case study with Al–Co–Cr–Fe–Ni system, Acta Mater. 192 (2020) 11–19. https://doi.org/10.1016/j.actamat.2020.03.039.
- [29] S. Guo, C.T. Liu, Phase stability in high entropy alloys: Formation of solid-solution phase or amorphous phase, Prog. Nat. Sci. Mater. Int. 21 (2011) 433–446. https://doi.org/10.1016/S1002-0071(12)60080-X.
- [30] O.N. Senkov, J.D. Miller, D.B. Miracle, C. Woodward, Accelerated exploration of multi-principal element alloys with solid solution phases, Nat. Commun. 6 (2015) 1–10. https://doi.org/10.1038/ncomms7529.
- [31] A. Inoue, Stabilization of metallic supercooled liquid and bulk amorphous alloys, Acta Mater. 48 (2000) 279–306. https://doi.org/10.1016/S1359-6454(99)00300-6.
- [32] X. Yang, Y. Zhang, Prediction of high-entropy stabilized solid-solution in multi-component alloys, Mater. Chem. Phys. 132 (2012) 233–238. https://doi.org/10.1016/j.matchemphys.2011.11.021.
- [33] Y.F. Ye, Q. Wang, J. Lu, C.T. Liu, Y. Yang, Design of high entropy alloys: A single-parameter thermodynamic rule, Scr. Mater. 104 (2015) 53–55. https://doi.org/10.1016/j.scriptamat.2015.03.023.
- [34] J.H. Li, M.H. Tsai, Theories for predicting simple solid solution high-entropy alloys: Classification, accuracy, and important factors impacting accuracy, Scr. Mater. 188 (2020) 80–87. https://doi.org/10.1016/j.scriptamat.2020.06.064.
- [35] Y. Liu, T. Zhao, W. Ju, S. Shi, Materials discovery and design using machine learning, J Mater. 3 (2017) 159–177. https://doi.org/10.1016/j.jmat.2017.08.002.
- [36] J. Wei, X. Chu, X. Sun, K. Xu, H. Deng, J. Chen, Z. Wei, M. Lei, Machine learning in materials science, InfoMat. 1 (2019) 338–358. https://doi.org/10.1002/inf2.12028.
- [37] R. Ramprasad, R. Batra, G. Pilania, A. Mannodi-kanakkithodi, C. Kim, Machine learning in materials informatics: recent applications and prospects, Npj Comput. Mater. (2017). https://doi.org/10.1038/s41524-017-0056-5.
- [38] G.L.W. Hart, T. Mueller, C. Toher, S. Curtarolo, Machine learning for alloys, Nat. Rev. Mater. 6 (2021) 730–755. https://doi.org/10.1038/s41578-021-00340-w.
- [39] N. Islam, W. Huang, H.L. Zhuang, Machine learning for phase selection in multi-principal element alloys, Comput. Mater. Sci. 150 (2018) 230–235. https://doi.org/10.1016/j.commatsci.2018.04.003.
- [40] W. Huang, P. Martin, H.L. Zhuang, Machine-learning phase prediction of high-entropy alloys, Acta Mater. 169 (2019) 225–236. https://doi.org/10.1016/j.actamat.2019.03.012.
- [41] R. Li, L. Xie, W.Y. Wang, P.K. Liaw, Y. Zhang, High-Throughput Calculations for High-Entropy Alloys: A Brief Review, Front. Mater. 7 (2020) 1–12. https://doi.org/10.3389/fmats.2020.00290.
- [42] Y. Chen, J. Zhu, N. Qu, Y. Chen, Z. Lai, Y. Liu, J. Zhu, A. Zanin, The phase selection via machine learning in high entropy alloys, Procedia Manuf. 37 (2019) 299–305. https://doi.org/10.1016/j.promfg.2019.12.051.
- [43] A. Agarwal, A.K. Prasada Rao, Artificial Intelligence Predicts Body-Centered-Cubic and Face-Centered-Cubic Phases in High-Entropy Alloys, Jom. 71 (2019) 3424–3432. https://doi.org/10.1007/s11837-019-03712-4.
- [44] F. Tancret, I. Toda-Caraballo, E. Menou, P.E.J. Rivera Díaz-Del-Castillo, Designing high entropy alloys employing thermodynamics and Gaussian process statistical analysis, Mater. Des. 115 (2017) 486–497. https://doi.org/10.1016/j.matdes.2016.11.049.
- [45] Y.V. Krishna, U.K. Jaiswal, R.M. R, Machine learning approach to predict new multiphase high entropy alloys, Scr. Mater. 197 (2021) 113804. https://doi.org/10.1016/j.scriptamat.2021.113804.
- [46] D.Q. Zhao, S.P. Pan, Y. Zhang, P.K. Liaw, J.W. Qiao, Structure prediction in high-entropy alloys with machine learning, Appl. Phys. Lett. 118 (2021). https://doi.org/10.1063/5.0051307.
- [47] Z. Pei, J. Yin, J.A. Hawk, D.E. Alman, M.C. Gao, Machine-learning informed prediction of high-entropy solid solution formation: Beyond the Hume-Rothery rules, Npj Comput. Mater. 6 (2020). https://doi.org/10.1038/s41524-020-0308-7.
- [48] Y. Zeng, M. Man, K. Bai, Y.W. Zhang, Revealing high-fidelity phase selection rules for high entropy alloys: A combined CALPHAD and machine learning study, Mater. Des. 202 (2021) 109532. https://doi.org/10.1016/j.matdes.2021.109532.

- [49] R. Machaka, Machine learning-based prediction of phases in high-entropy alloys, Comput. Mater. Sci. 188 (2021) 110244. https://doi.org/10.1016/j.commatsci.2020.110244.
- [50] L. Zhang, H. Chen, X. Tao, H. Cai, J. Liu, Y. Ouyang, Q. Peng, Y. Du, Machine learning reveals the importance of the formation enthalpy and atom-size difference in forming phases of high entropy alloys, Mater. Des. 193 (2020) 108835. https://doi.org/10.1016/j.matdes.2020.108835.
- [51] Z. Zhou, Y. Zhou, Q. He, Z. Ding, F. Li, Y. Yang, Machine learning guided appraisal and exploration of phase design for high entropy alloys, Npj Comput. Mater. 5 (2019) 1–9. https://doi.org/10.1038/s41524-019-0265-1.
- [52] Y. Zhang, Y.J. Zhou, J.P. Lin, G.L. Chen, P.K. Liaw, Solid-solution phase formation rules for multi-component alloys, Adv. Eng. Mater. 10 (2008) 534–538. https://doi.org/10.1002/adem.200700240.
- [53] Y. Zhang, X. Yang, P.K. Liaw, Alloy design and properties optimization of high-entropy alloys, Jom. 64 (2012) 830–838. https://doi.org/10.1007/s11837-012-0366-5.
- [54] M.G. Poletti, L. Battezzati, Electronic and thermodynamic criteria for the occurrence of high entropy alloys in metallic systems, Acta Mater. 75 (2014) 297–306. https://doi.org/10.1016/j.actamat.2014.04.033.
- [55] S. Fang, X. Xiao, L. Xia, W. Li, Y. Dong, Relationship between the widths of supercooled liquid regions and bond parameters of Mg-based bulk metallic glasses, J. Non. Cryst. Solids. 321 (2003) 120–125. https://doi.org/10.1016/S0022-3093(03)00155-8.
- [56] A. Takeuchi, I. Akihisa, Classification of bulk metallic glasses by atomic size difference, heat of mixing and period of constituent elements and its application to characterization of the main alloying element, Mater. Trans. 46 (2005) 2817–2829. https://doi.org/10.2320/matertrans.46.2817.
- [57] A. Takeuchi, A. Inoue, Quantitative evaluation of critical cooling rate for metallic glasses, Mater. Sci. Eng. A. 304–306 (2001) 446–451. https://doi.org/10.1016/S0921-5093(00)01446-5.
- [58] A.R. Miedema, P.F. de Châtel, F.R. de Boer, Cohesion in alloys fundamentals of a semiempirical model, Phys. B+ C. 100 (1980) 1–28. https://doi.org/10.1016/0378-4363(80)90054-6.
- [59] F. Pedregosa, R. Weiss, M. Brucher, Scikit-learn: machine learning in python, J. Mach. Learn. Res. 12 (2011) 2825–2830.
- [60] S.R. Safavian, D. Landgrebe, A survey of decision tree classifier methodology, IEEE Trans. Syst. Man Cybern. 21 (1991) 660–674. https://doi.org/10.1109/21.97458.
- [61] D.E. Knuth, Optimum binary search trees, Acta Inform. 1 (1971) 14–25. https://doi.org/10.1007/BF00264289.
- [62] T.M. Cover, P.E. Hart, Nearest neighbor pattern classification, IEEE Trans. Inf. Theory. 13 (1967) 21–27. https://doi.org/10.1109/TIT.1967.1053964.
- [63] J.M. Keller, M.R. Gray, A Fuzzy K-Nearest Neighbor Algorithm, IEEE Trans. Syst. Man Cybern. 4 (1985) 580–585. https://doi.org/10.1109/TSMC.1985.6313426.
- [64] P.E. Danielsson, Euclidean distance mapping, Comput. Graph. Image Process. 14 (1980) 227–248. https://doi.org/10.1016/0146-664X(80)90054-4.
- [65] C. Cortes, V. Vapnik, Support-vector networks, Mach. Learn. 20 (1995) 273–297. https://doi.org/10.1023/A:1022627411411.
- [66] R.P. Lippmann, An introduction to computing with neural nets, IEEE ASSP Mag. 4 (1987) 4–22. https://doi.org/10.1109/MASSP.1987.1165576.
- [67] L.K.A.I. Hansen, P. Salamon, Neural network ensembles, IEEE Trans. Pattern Anal. Mach. Intell. 12 (1990) 993–1001.
- [68] Y. Li, W. Guo, Machine-learning model for predicting phase formations of high-entropy alloys, Phys. Rev. Mater. 3 (2019) 095005. https://doi.org/10.1103/PhysRevMaterials.3.095005.
- [69] H. Wu, A. Lorenson, B. Anderson, L. Witteman, H. Wu, B. Meredig, D. Morgan, Robust FCC solute diffusion predictions from ab-initio machine learning methods, Comput. Mater. Sci. 134 (2017) 160–165. https://doi.org/10.1016/j.commatsci.2017.03.052.
- [70] Y. Zhang, C. Wen, C. Wang, S. Antonov, D. Xue, Y. Bai, Y. Su, Phase prediction in high entropy alloys with a rational selection of materials descriptors and machine learning models, Acta Mater. 185 (2020) 528–539. https://doi.org/10.1016/j.actamat.2019.11.067.
- [71] J.-C. Zhao, M.F. Henry, CALPHAD Is it ready for superalloy design?, Adv. Eng. Mater. 4 (2002) 501–508. https://doi.org/10.1002/1527-2648(20020717)4:7<501::AID-ADEM501>3.0.CO;2-3.

- [72] R. Raghavan, K.C. Hari Kumar, B.S. Murty, Analysis of phase formation in multi-component alloys, J. Alloys Compd. 544 (2012) 152–158. https://doi.org/10.1016/j.jallcom.2012.07.105.
- [73] A. Mangal, E.A. Holm, A comparative study of feature selection methods for binary text streams classification, Integr. Mater. Manuf. Innov. 7 (2020) 87–95. https://doi.org/10.1007/s12530-020-09357-y.
- [74] D.J.M. King, S.C. Middleburgh, A.G. McGregor, M.B. Cortie, Predicting the formation and stability of single phase high-entropy alloys, Acta Mater. 104 (2016) 172–179. https://doi.org/10.1016/j.actamat.2015.11.040.